Journal of Nano- and Electronic Physics
Vol. **17** No 6, 06038(10pp) (2025)

Журнал нано- та електронної фізики
Том **17** № 6, 06038(10cc) (2025)

OPEN ACCESS

REGULAR ARTICLE

Tailoring Hemp-Derived Porous Carbon through Chemical Activation: Fractal Dimension Analysis and Capacitive Properties

R.I. Zapukhlyak*, V.O. Kotsyubynsky†, V.M. Boychuk, V.T. Hoi, M.M. Klymyuk

Vasyl Stefanyk Carpathian National University, 76018 Ivano-Frankivsk, Ukraine

(Received 28 July 2025; revised manuscript received 16 December 2025; published online 19 December 2025)

This study investigates the structural and electrochemical properties of hemp fiber-derived porous carbon materials synthesized through steam-assisted carbonization (C series) and nitric acid activation (CN series). The CN series exhibited higher microporosity and a narrow pore size distribution (centered around 2-3 nm), while the C series demonstrated a broader micro-mesoporous structure. Fractal dimensions calculated using SAXS and FHH methods showed consistent trends, with the C series revealing a positive correlation at the mesopore scale and the CN series highlighting the dominance of microporous arrangements. Electrochemical evaluations showed the CN series materials achieving good specific capacitance and rate capabilities due to their optimized pore structure and surface functionalization, enabling a substantial pseudocapacitive contribution. In contrast, the C series primarily relied on double-layer capacitance, supported by its mixed micro-mesoporous structure. The study highlights the influence of synthesis methods on tailoring pore architecture and functional performance, providing insights into designing porous carbon materials for advanced applications such as energy storage, catalysis, and adsorption.

Keywords: Porous carbon, SAXS, Porosimetry, Fractal dimension, Pore distribution, Specific capacitance.

DOI: 10.21272/jnep.17(6).06038 PACS numbers: 61.43.Gt, 68.43.Bc

1. INTRODUCTION

Porous carbon materials, owing to their unique combination of physical and chemical properties, are highly versatile systems used in diverse fields ranging from medicine to nanoelectronics. These materials meet essential criteria such as low cost, environmental friendliness, and technological adaptability.

Structurally, porous carbon materials are often found in an X-ray amorphous or near-amorphous state. Their particles result from the agglomeration or sintering of individual turbostratically organized graphene layer packets, where both sp^2 and sp^3 hybridization of carbon-carbon bonds coexist [1]. The disordered cross-linking bonds that connect individual graphene plane packets (graphitic crystallites) confer stability to graphitization during thermal processing, influencing the mechanical properties and pore size distribution. These transitional zones form clusters dominated by tetrahedral bonds between carbon atoms, with sp^3 bonds detectable using Raman spectroscopy. Franklin's model predicts the reorganization and growth of individual graphene layer packets during thermal treatment due to the surrounding X-ray amorphous material [2]. The size of individual packets in partially graphitized carbon material along the (002) plane normal direction is up to 3-4 nm, with lateral dimensions up to about 20 nm. These packets contain 3-10 graphene layers, which are randomly oriented relative to one another [3]. Increasing temperature induces partial spatial separation of crystalline and amorphous regions. Individual graphitic particles exhibit a framework formed by covalently bonded graphene layer packets, with interlayer distances exceeding typical graphite values ($d_{(002)} = 0.335$ nm) by 5-15 %, reaching 0.35-0.37 nm or more.

The structure of carbon materials consists of randomly oriented flat-parallel graphene planes linked by short aliphatic radicals. The average crystallite size depends on the material type, synthesis conditions, and preparation method. Functional groups of various types (passive and active) may reside on the surfaces and edges of these planes, determining the physical-chemical and catalytic properties of the carbon material [4]. Passive structural elements include hydrogen and hydrocarbon fragments of aliphatic and aromatic character without heteroatoms. Although passive groups do not directly participate in adsorption processes, they significantly influence the distribution of electronic density in the graphene plane, defining the donor-acceptor properties of the carbon material. Active structural elements, such as oxygen-containing groups (e.g., –COR, –COOH, –OH) and heteroatom-based groups (e.g., $–SO_3H$, $–NO_2$), directly affect electronic density distribution and sharply alter material properties. For example, functionalized carbon used as an electrode material benefits from the high electrochemical activity of these groups, enabling rapid redox reactions for charge storage via pseudo-capacitive mechanisms [5]. Surface functional groups also enhance the electrical conductivity of carbon materials [6].

The type and concentration of functional groups and

* Correspondence e-mail: ruslan.zapukhlyak@pnu.edu.ua
† volodymyr.kotsuybynsky@pnu.edu.ua

Cite this article as: R.I. Zapukhlyak et al., *J. Nano- Electron. Phys.* 17 No 6, 06038 (2025) https://doi.org/10.21272/jnep.17(6).06038

heteroatoms (oxygen, nitrogen, sulfur, hydrogen) can be controlled by varying the synthesis and post-treatment conditions [7]. Such control enables the production of surface-modified carbon materials suitable for specific adsorption or electrochemical applications. Recent studies have demonstrated the potential of hemp fiber as a sustainable precursor for carbon materials. The carbonization of hemp fibers results in materials with enhanced porosity and surface properties, making them suitable for various adsorption and electrochemical applications. For instance, carbonized hemp fibers have been successfully applied as solid-phase extraction sorbents for pesticide analysis in water [8]. Other studies have linked the synthesis conditions of hemp-derived carbons to their capacitive properties, revealing their potential as supercapacitor materials [9]. Furthermore, chemical activation of hemp-derived carbons has been shown to significantly enhance their adsorption capacities, particularly for environmental applications [10]. These findings highlight the versatility of hemp fibers as a precursor for advanced carbon materials.

2. MATERIALS AND METHODS

2.1 Synthesis of Porous Carbon Materials

The C series materials (C600, C700, C800, C900) were synthesized via steam-assisted carbonization. Mechanically ground hemp fiber was used as the primary biomass source. The fiber was placed in a high-pressure reactor filled with distilled water. The reactor environment was maintained under saturated steam conditions with a pressure range of 6-8 × 10^5 Pa. The temperature was ramped at a controlled rate of 8-10 °C/min to reach the target carbonization temperatures (600-900 °C). Once the target temperature was reached, the material underwent an isothermal hold for 3 hours to allow complete carbonization. The reactor was subsequently cooled naturally to ambient temperature. The obtained samples were labeled as CX, where X denotes the carbonization temperature (e.g., C600, C700, etc.). This process results in a dense carbon material with relatively smooth surfaces and minimal porosity, primarily governed by the initial biomass composition and reaction conditions.

The CN series materials (CN600, CN700, CN800, CN900) were derived from the C series samples through chemical activation using nitric acid. Pre-carbonized C series materials were mixed with a 65 % aqueous nitric acid solution in a 1:1 volume ratio and subjected to boiling conditions for 3 hours with continuous stirring. This process facilitated the etching of carbon surfaces and the introduction of oxygen-containing functional groups. After activation, the reaction mixture was cooled, and the solid precipitate was washed thoroughly with distilled water until the pH of the filtrate exceeded 5.0.

The washed samples were air-dried at 65 °C. The resulting CN series materials were labelled as CNX, where X represents the initial carbonization temperature. The nitric acid activation step significantly increased the porosity and surface heterogeneity of the CN samples, enabling the development of hierarchical pore structures and active surface sites suitable for adsorption and catalytic applications.

2.2 Characterization Techniques

XRD analyses were conducted using a Shimadzu XRD-7000 diffractometer with Cu Kα radiation (λ = 1.5418 Å). The X-ray tube was operated at a voltage of 30 kV and a current of 40 mA to investigate the crystallographic structure and interlayer distances in the carbon materials. SAXS measurements were performed using the same Shimadzu XRD-7000 diffractometer. This method was used to determine fractal dimensions and analyze hierarchical pore structures within the samples. Morphological characteristics of the obtained carbon materials were analyzed via low-temperature (77 K) nitrogen adsorption-desorption isotherms using a Quantachrome Autosorb Nova 2200e system. Preliminary degassing of the samples was conducted at a temperature of 180 °C for 12-14 hours. Pore size distribution and surface area calculations were carried out with the NovaWin software package. Cyclic voltammograms were measured using Autolab PGSTAT12 galvanostat-potentiostat with GPES and FRA-2 software.

3. RESULTS AND DISCUSSION

3.1 XRD Analysis

The XRD patterns for the C and CN series are shown in Fig. 1 a-b, respectively. Both series exhibit two primary diffraction peaks: at $2\theta \approx 23°$, corresponding to the (002) plane of turbostratic carbon, and near 2θ of 43°, corresponding to the (10) plane. The (10) peak results from the overlapping of the (100) and (101) diffraction planes of a distorted graphite lattice. Analysis of the diffractograms involved approximating the peaks using Lorentzian fitting to determine the angular positions of the (002) and (10) peaks and their full-width at half-maximum (FWHM) values.

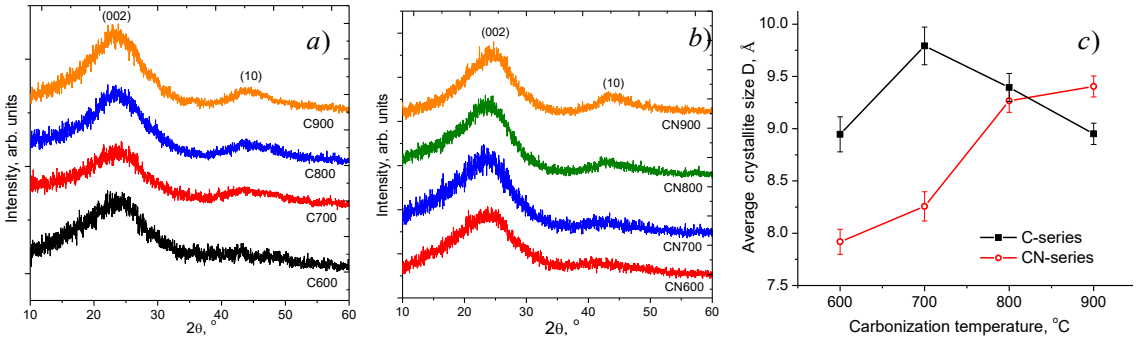

Fig. 1 – XRD patterns of (a) C- and (b) CN-series of porous carbon materials; (c) variation of average crystallite size (D_{002}) with carbonization temperature for both sample series

The interplanar spacing d_{002} was approximately 0.37 nm for all C-series samples, regardless of carbonization temperature. Similar values were observed for the CN-series samples carbonized at 600-700 °C. Slight decrease in d_{002} to 0.365 nm was observed for CN800 and CN900 materials. Fig. 1c illustrates the variation of the average crystallite size D_{002} in the direction normal to the (002) crystal plane calculated using the Scherrer equation as a function of carbonization temperature for both C- and CN-series materials.

C-series exhibits a peak crystallite size at 700 °C, followed by a decline at higher temperatures. In contrast, the CN-series demonstrates a gradual increase in crystallite size with rising carbonization temperatures, reaching values comparable to the C series at 900 °C. The largest average crystallite sizes (D_{002}) for the C-series samples were observed for C700 (of about 9.8 Å). Further increases in carbonization temperature caused a linear decrease in D_{002} to 8.5 Å for C900. After nitric acid treatment, a reduction in D_{002} to 8 Å was observed for CN samples carbonized at 500-700 °C, while higher temperatures led to an increase in to about 9 Å. The average number of graphene layers per crystallite for both series was approximately 3.5.

3.2 SAXS

Fractal dimensions of carbon materials are an essential integral parameter characterizing the structure and spatial organization of such materials. This parameter allows for determining how evenly the mass is distributed in the carbon material and to what extent its surface is rough or porous [11]. In the context of carbon materials, the fractal dimension may indicate structural features, such as the presence of porous, fibrous aggregates of particles (characteristic of carbon derived from plant materials, particularly hemp fibers) or complex nanostructures [12].

The calculation of the fractal dimension using SAXS is based on analyzing of a normalized scattering intensity I as a function of the diffraction vector modulus s: $I(s) = f(s^{-n})$. The slope of this dependence in in logarithmic scale determines the fractal dimension, which can vary between 1 and 4. For the case of $3 < n < 4$, scattering occurs by particles with a surface fractality (fractal dimension) equal to 6-n, while at $1 < n < 3$, the presence of fractal aggregates (clusters) with dimension $D = n$ in the interval $L_0^{-1} >> s >> L$ is expected, where L_0 and L are the minimum size of individual particles in the cluster and the size of the entire cluster, respectively. The value of $D = 4$ corresponds to the Porod's law for X-ray scattering by homogeneous particles with linear dimensions L and a smooth surface under the condition $sL >> 2\pi$. For cases of synthesized carbons (Fig. 2) Log(I) vs log(s) dependencies are characterized by linear regions on the lg(I) vs lg(s) dependence, reflecting contributions from surface and bulk fractal structures. For microporous (pores with the sized < 2 nm) the range of s is about 0.1-0.01 A^{-1}, for mesoporous (pore size in a range of 2-50 nm) $s \approx 0.001$-0.01 A^{-1} [13]. The fractal dimensions FD_{SAXS} derived from SAXS analysis for the C and CN series materials as a function of carbonization temperature reveal distinct trends between the two series (Fig. 3). For the CN series, the consistent increase in fractal dimensions with temperature highlights the role of chemical activation in developing complex, hierarchical structures. At higher carbonization temperatures, the introduction of nanoscale pores and structural heterogeneity becomes pronounced, contributing to fractal complexity.

Conversely, the C series shows a decreasing trend in fractal dimensions with rising temperatures, suggesting that steam-assisted carbonization leads to more compact and uniform structures, with a reduction in surface and bulk heterogeneity. This trend suggests that nitric acid activation plays a critical role in increasing the surface roughness and introducing nanoscale heterogeneities [14]. In contrast, the fractal dimension of C-series materials decreases with increasing temperature, reflecting a transition to smoother and more uniform structures at higher carbonization temperatures.

This behavior highlights the contrasting effects of thermal carbonization and chemical activation processes on the structural evolution of carbon materials. The results emphasize that the synthesis conditions strongly influence the surface and bulk fractal properties of the materials, with significant implications for their potential applications in adsorption, catalysis, and energy storage systems.

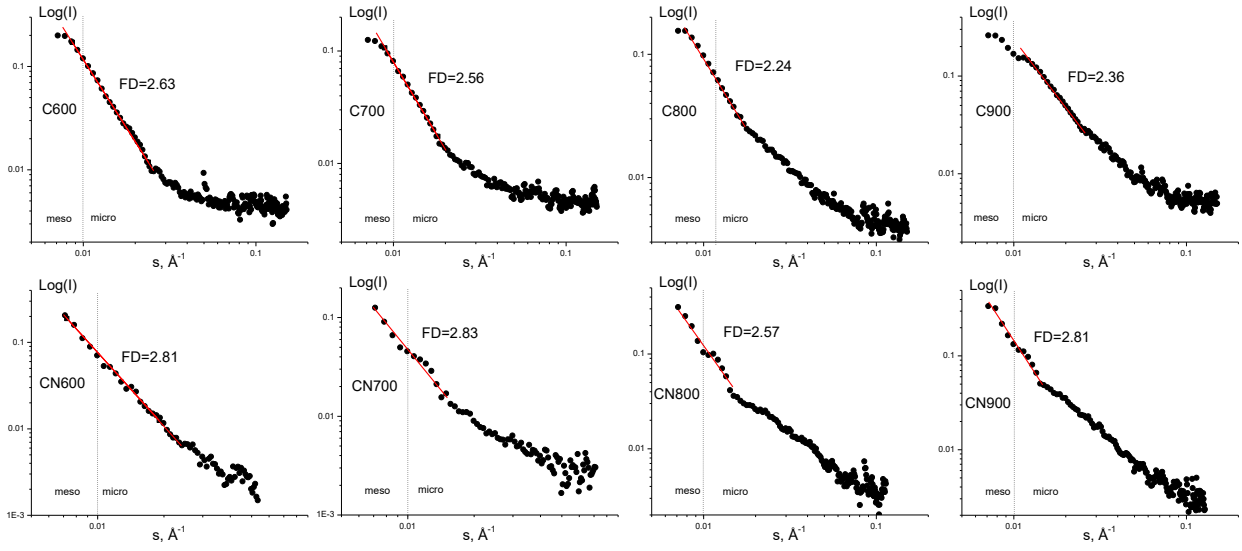

Fig. 2 – SAXS dependencies Log(I) = f(log(s)) for carbons of C- and CN-series (experimental data and the result of linearization)

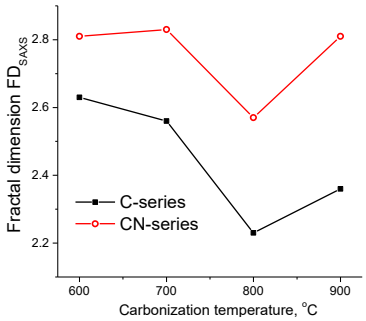

Fig. 3 – SAXS derived fractal dimensions of carbon materials of C- and CN-series

3.3 Porometry

Figure 4 presents the nitrogen adsorption-desorption isotherms (dependence of the volume of adsorbed nitrogen in cm^3/g as a function of the relative pressure, where p_0 is the saturated vapor pressure of nitrogen at 77 K) for porous carbons of C- and CN- series. All isotherms of C-series exhibit a typical form characteristic of mesoporous materials, with a stable increase in adsorption volume with increasing relative pressure in all cases, indicating a well-developed porous structure. The isotherms can be classified as Type IV according to the IUPAC classification, characterized by initial adsorption in micropores at low values, the presence of a hysteresis loop in the medium range (p/p_0 = 0.4-1.0), indicating the presence of mesopores, and an increase in adsorption volume at close to 1 (indicative of the gradual filling of mesopores due to capillary condensation) [15]. According to the IUPAC classification, the hysteresis loops for C-series materials carbonized at temperatures of 600-700 °C belong to Type H2b associated with the presence of disordered/ irregular network of interconnected pores with narrow necks and wide bodies ("ink-bottle" pores) [16]. The shape of the hysteresis suggests that the pores in these materials have a non-uniform size distribution. C800 and C700 samples demonstrate larger adsorption volumes at higher relative pressures compared to C900 and C600, implying larger pore volumes. C900 shows a narrower hysteresis loop, which suggests a reduction in mesopore size or structural changes due to higher activation temperatures. The observed differences are likely due to the impact of activation temperature on pore structure. Higher activation temperatures, as in C900, may lead to pore collapse or transformations. In contrast, lower temperatures, as in C600, result in less developed pore structures, whereas intermediate temperatures, as seen in C800 and C700, produce optimal pore structures with larger volumes and surface areas.

The typical Type IV isotherms obtained for CN-series carbon materials indicate its mesoporous structure have a distinct hysteresis loops resembling Type H1 or H2b, indicative of uniform ink-bottle-shaped pores. The adsorption volume increases with relative pressure (p/p_0), reflecting the filling of mesopores, and higher adsorption volumes in samples such as CN800 and CN900 suggest greater mesoporosity or better pore accessibility. In contrast, CN700 shows lower adsorption volumes, indicating smaller pore volumes CN800 and CN900 samples exhibit broader hysteresis loops, likely due to more interconnected or larger mesopores. The presence of microporosity is also suggested by significant adsorption at lower relative pressures, which contributes to the overall surface area.

The dependence of BET specific surface area (S_{BET}) on carbonization temperature for the C and CN series carbon materials (Fig.5a) shows distinct trends. Both series exhibit an increase in S_{BET} with rising carbonization temperature, peaking at approximately 800 °C, followed by a decline at higher temperatures. The CN series reaches a significantly higher maximum S_{BET}, approximately 1400 m^2/g, compared to the C series, which peaks at around 900 m^2/g. This indicates that the CN series undergoes more efficient pore development, possibly due to differences in feedstock composition or activation conditions. At lower temperatures (500-700 °C), S_{BET} increases gradually as initial pore formation takes place. However, beyond 800 °C, the specific surface area decreases, likely due to pore collapse or densification caused by thermal treatment Another possible reason is the BET model based on the Langmuir adsorption. BET struggles to accurately describe micropore behavior because it assumes multilayer adsorption, which is not applicable when micropore filling dominate. NLDFT method was used for determining the pore surface area (S_{DFT}) and pore size distribution for obtained carbon materials in assumption of cylindrical pores.

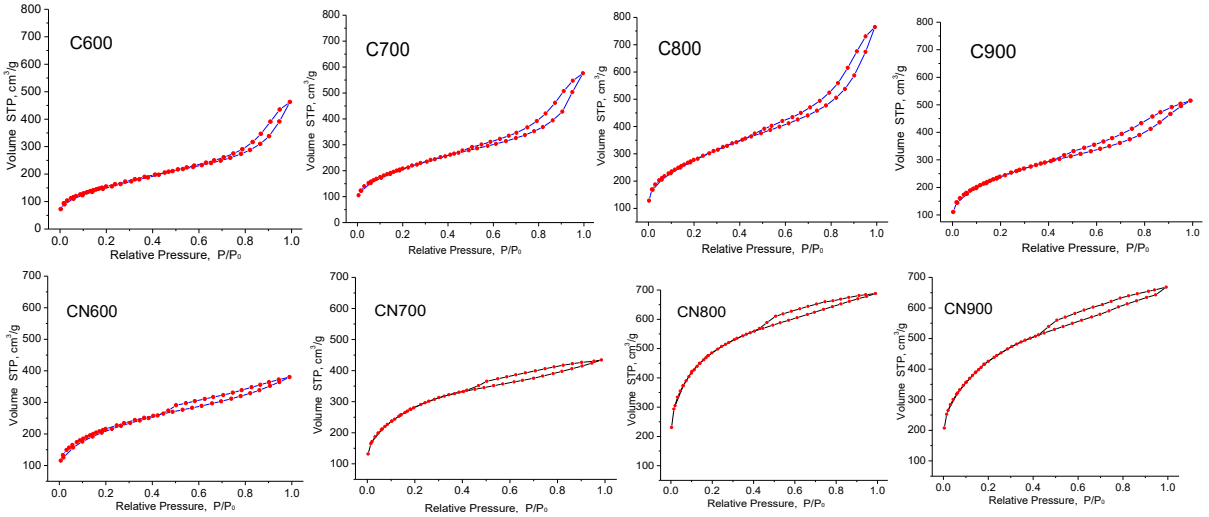

Fig. 4 – Nitrogen adsorption-desorption isotherms of the C- and CN series carbon materials

Unlike BET, NLDFT approach can provides more accurate results for synthesized carbons with significant microporosity and irregular pores with taking into consideration the effects of pore geometry [17].

The calculated values of S_{BET} exceed S_{DFT} and its typical for materials with significant microporosity and complex pore structures. (Fig. 5b). For the C-series S_{DFT} shows a modest increase with a slight plateau at 900 °C, mirroring the changes of S_{BET} (Fig. 5a). S_{DFT} values for the CN-series carbons increase consistently with carbonization temperature, without showing a peak, indicating a continuous development of micropores and the robustness of NLDFT in capturing microporosity. Calculated NLDFT distributions of S_{DFT} agree with this conclusion (Fig. 6).

The C-series carbon materials display a mix of micropores and mesopores, with a broader S_{DFT} distribution and significant surface area contribution from mesopores, particularly in C600 and C700. For C800 and C900 samples shift in the distribution is observed, with the peak surface area still at 2-3 nm but with reduced mesopores contributions, indicating a reduction in mesopore content. The CN-series materials exhibit narrower S_{DFT} distributions, with most of the surface area concentrated in pores with the sizes around 2 nm. Across the CN-series the peak surface area is consistently located at 2 nm with limited mesoporosity indicating a stable pore structure.

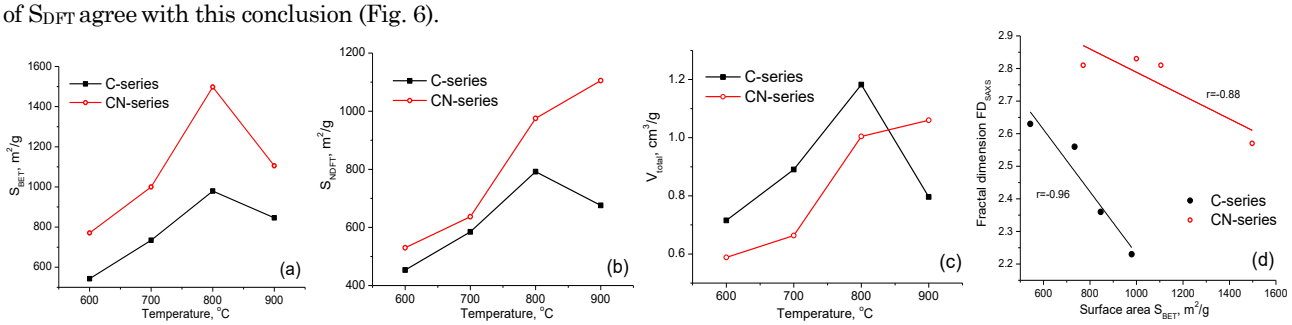

Fig. 5 – Dependences of (a) BET specific surface area (S_{BET}), (b) NLDFT specific surface area (S_{DFT}), (c) total NDFT pore volume as a function of carbonization temperature of the feedstock as well as (d) the correlation between S_{BET} and FD_{SAXS} for C and CN series carbon materials

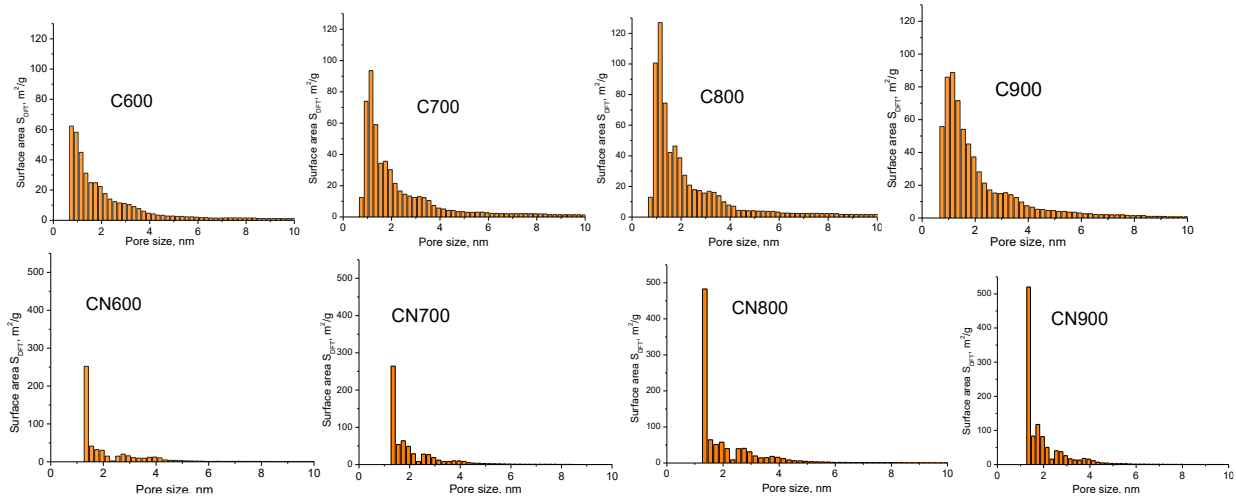

Fig. 6 – NLDFT specific surface area (SDFT) distributions for C- and CN series carbon materials

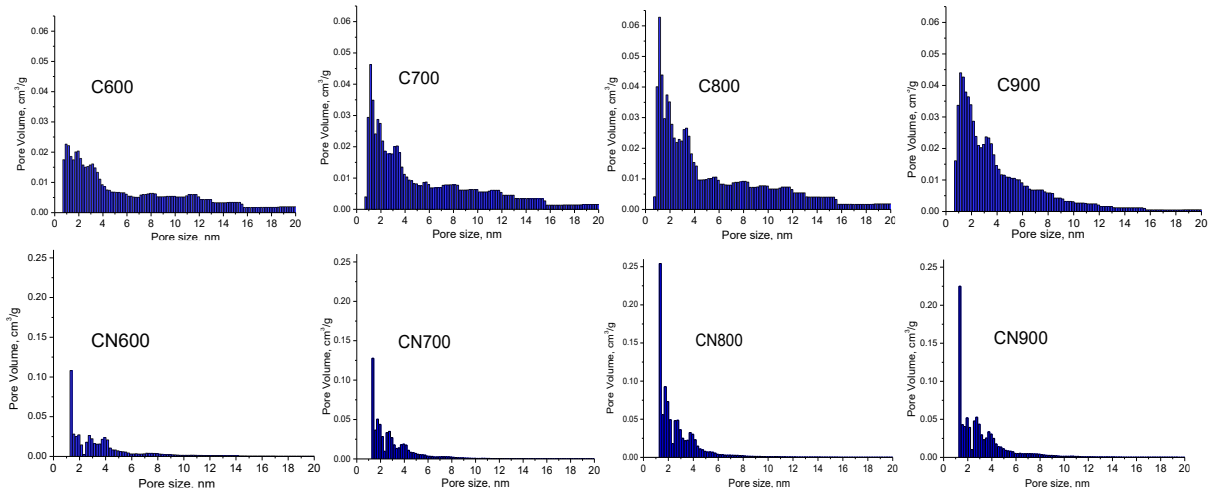

Fig. 7 – NLDFT pore size distributions) distributions for C- and CN series carbon materials

The total pore volume for the C-series (Fig. 5c) increases with carbonization temperature, reaching a peak at 800 °C, similar to S_{BET}. At 900 °C, the total pore volume decreases slightly, indicating that excessive carbonization may reduce the overall porosity by collapsing larger pores or shrinking the material structure. The CN-series shows a steady increase in total pore volume across the entire temperature range, with the highest volume observed at 900 °C. This increase indicates a continuous enhancement of pore development. The CN-series consistently exhibits lower total pore volume compared to the C-series across all temperatures. This suggests that the C-series materials have a more significant contribution from mesopores, while the CN-series is dominated by micropores, resulting in a lower overall pore volume but higher specific surface area at higher temperatures [18]. The strong negative correlations are observed between S_{BET} and FD_{SAXS} both for C-series ($r = -0.96$) and CN-series ($r = -0.86$) carbon materials reflect the inverse relationship between surface area and structural complexity (Fig. 5d). S_{BET} measures the accessible surface area, which is typically higher in materials with smoother and more uniform pore structures. In contrast, FD_{SAXS} quantifies the structural complexity, including surface roughness and pore irregularities. Materials with high fractal dimensions have more complex and irregular surfaces, which can reduce the effective surface area available for gas adsorption.

Higher surface area is associated with well-developed micropores/mesopores, which tend to have lower structural complexity. Conversely, materials with higher fractal dimensions often exhibit irregular or hierarchical pore structures that limit the accessible surface area [19]. The pore size distributions for C-series materials demonstrate a broad range of pore sizes with contribution to pore volume both from micro- and mesopores (Fig. 7).

Pore development peaks at temperatures of 800 °C, where mesopore content is maximized. At higher temperatures (C900 sample) structural collapse leads to a reduction in mesoporosity. The CN-series materials are predominantly microporous and exhibit a narrow pore size distribution centered around 2-3 nm. C800 sample demonstrate the highest pore volume, after which the pore stabilizes or decreases slightly. For the calculation of fractal dimensions based on porometry data, the Frenkel–Halsey–Hill (FHH) model was applied [20]. The FHH model analyzes adsorption isotherms and allows for the determination of the fractal dimension (D) by evaluating the relationship between the volume of adsorbed gas (V) and relative pressure for adsorption on heterogeneous surfaces using the equation: $\ln(V) = K \cdot \ln(\ln(p_0/p)) + C$, where $K = 3\text{-FD}$ is a parameter associated with the fractal dimension FD, and C is a constant dependent on the material and adsorbate. FD values were determined using linear regression of the linear region on the dependence of $\ln(V)$ on $\ln(\ln(p_0/p))$ (Fig. 8).

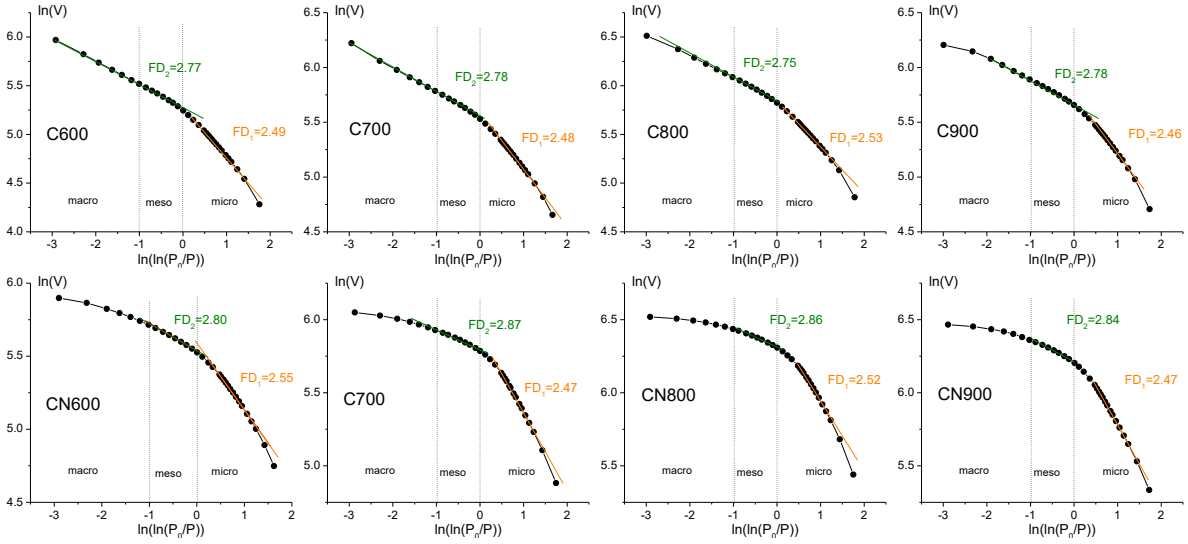

Fig. 8 – Frankel-Holsey-Gill plots for C- and CN-series of carbon materials, as well as a diagram of changes in the fractal dimension of these materials as a function of carbonization temperature

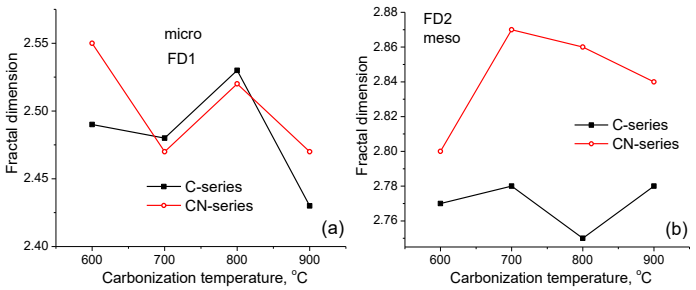

Fig. 9 – The fractal dimensions of C and CN carbons calculated by the FHH in the ranges (a) from 0.5 to 1.5 (micropores) and (b) from – 1 to 0.5 (mesopores)

The FHH model is designed to analyze adsorption processes in micropores and mesopores. In macropores adsorption occurs via multilayer adsorption or physical filling, rather than capillary condensation that leads unreliable fractal dimension estimates. It can be approximately suggesting the association $\ln(\ln(p_0/p)) > 0$ with micropores range and $-1 \le \ln(\ln(p_0/p)) \le 0$ with mesopores range. Fractal dimensions derived using the FHH method across "micro" (FD_1) and "meso" (FD_2) ranges of $\ln(\ln(p_0/p))$ for the C and CN series materials are presented on Fig 9. FD_1 values for the C-series are changing in a range of 2.43-2.55, decrease slightly with increasing carbonization temperature from 600 °C to 700 °C, followed by a peak at 800 °C and a drop at 900 °C (Fig. 9a). The peak at 800 °C can be associated with maximal micropore irregularity, corresponding to a high degree of pore development and the highest values of S_{BET}, S_{DFT} and total pores volume (Fig. 5).

The decline at 900 °C suggests some structural smoothing, reducing the fractal nature of micropores. For the CN-series the changes of FD_1 values is very close to observed for C-series materials. Similar to the C-series, the peak at 800 °C reflects the most developed microporous structure in terms of fractal complexity. Fractal dimension values at mesopore range (FD_2) for the C-series show minimal fluctuation on a range 2.75-2.77 across the carbonization temperature range, that suggests stability of mesopore arrangement. For the CN-series, FD_2 increases significantly from 600 °C to 700 °C, reaches a peak at 800 °C, and then decreases at 900 °C (Fig. 9b). This trend indicates that mesopore complexity and irregularity are more strongly differs for materials after acid activation. The CN-series materials demonstrate higher FD_2 across all temperature ranges for mesopores and the similar tendency for micropores indicating more complex structures, compared to the C-series. These results agree with FD_{SAXS} data (Fig. 3). The strong positive correlation ($r = 0.59$) is observed between fractal dimensions for mesopore ranges calculated using SAXS and FHH data for C series. A similar dependence is not observed for CN series carbons where the contribution of micropores is dominant.

3.4 CVA Analysis

The electrochemical properties of C and CN carbons were analyzed using cyclic voltammetry (CV) in a three-electrode cell configuration, with Ag/AgCl as the reference electrode, a platinum plate as the counter electrode and 6 M aqueous KOH as electrolyte. Working electrode was prepared by applying aqueous slurry containing 87 wt. % carbon material, 10 wt. % Super P carbon black, and 3 wt. % PVDF on the thermally expanded graphite foil. The coated foil (working area approximately 1.5 cm², thickness of 1 mm) was vacuum-dried for 5-6 hours. CV measurements were performed at scan rates ranging from 1 to 40 mV/s for both the initial (C-series) and nitric acid-treated (CN-series) carbon materials (Fig. 10). CV curves for both series reveal a quasi-rectangular shape at low scan rates for both series, indicating an electrostatic charge storage mechanism. As the scan rate increases, the deformation of the quasi-rectangular shape becomes more pronounced, reflecting ion transport limitations and reduced accessibility to smaller pores. This behavior underscores the importance of pore structure in determining ion diffusion efficiency and charge storage capacity [21]. The differences between the CV curves for C- and CN-series carbons at a scan rate of 1 mV/s are primarily attributed to the effects of synthesis and activation processes (Fig. 11a-b). The CN-series carbons, modified through nitric acid activation, exhibit hierarchical porosity that enhances ion transport pathways. The surface functionalization of CN-series carbons with nitrogen-containing functional groups enhance surface wettability, facilitating electrolyte access and supporting pseudocapacitive charge storage with higher electrical conductivity, ensuring faster electron transport during the charge-discharge process [22].

The C-series carbons with less-developed meso- and microporous structures lacking such functionalization, rely primarily on electrostatic double-layer capacitance, resulting in comparatively lower current densities and reduced CV areas. The specific capacitance of the materials was calculated from the CV data as follows: $C = \int_{U_1}^{U_2} I(U)\,dU \Big/ ms(U_2 - U_1)$, where U_1 and U_2 are the cutoff potentials in cyclic voltammetry, $I(U)$ is the instantaneous current, m is the mass of carbon materials, s is the scan sweep rate. The CN series demonstrates higher specific capacitance across all scan rates compared to the C series (Fig. 11c-d).

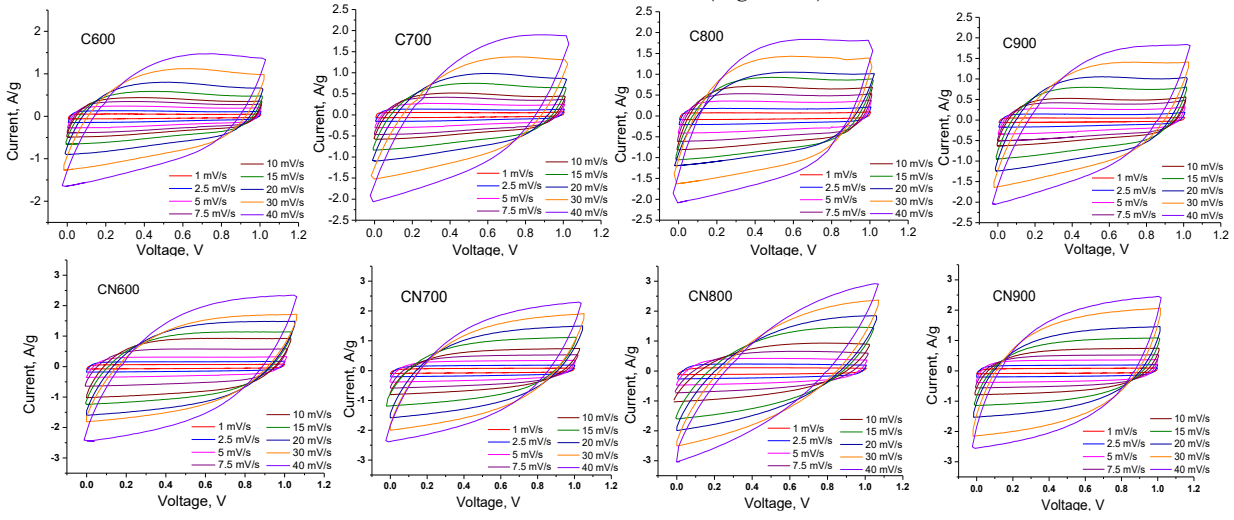

Fig. 10 – CV curves measured for electrodes based on the C- and CN-carbons at scan sweep rate 1-40 mV/s (6 M KOH electrolyte)

This performance can be attributed to the hierarchical pore structure and increased surface heterogeneity introduced by nitric acid activation, which enhances ion accessibility and facilitates charge storage [23]. At low scan rates, the CN series materials achieve near-complete utilization of their active surface area due to effective ion diffusion into micropores and mesopores. However, as the scan rate increases, the decline in capacitance becomes more pronounced for both series, primarily due to restricted ion diffusion and limited accessibility to smaller or poorly connected pores.

The exponential decline in specific capacitance with increasing scan rate is primarily attributed to ion accessibility limitations within the porous structure of the electrode material. At low scan rates, ions in the electrolyte have sufficient time to diffuse into the micropores and mesopores, allowing full utilization of the active surface area for charge storage. However, as the scan rate increases, the time available for ion diffusion becomes insufficient, restricting access to smaller or less connected pores. Consequently, only the larger pores and the external surface of the material contribute to the capacitance at high scan rates.

This behavior is further compounded by the inability of ions to rearrange and form a stable double layer or participate in pseudocapacitive redox processes under rapid voltage sweeps, resulting in incomplete charge storage. The tortuous pathways and varying connectivity of the porous network exacerbate this limitation, as small or poorly connected micropores become less accessible at higher scan rates. The resistance within the electrolyte and the electrode leads to a larger voltage drop at high scan rates, reducing the effective potential window for charge storage.

The extent of capacitance decline also depends on the material properties, including electrical conductivity and pore size distribution. Materials with high conductivity and an optimized balance of mesopores and micropores demonstrate better rate capabilities and smaller capacitance losses at higher scan rates. This underscores the importance of designing materials with interconnected pore networks and enhanced conductivity to maximize ion accessibility and mitigate the decline in capacitance under operating conditions [24].

The experimental dependences of specific capacitance on scan rate were fitted declining exponential function, expressed as $C(s) = C_\infty + (C_0 - C_\infty)\exp[-ks]$, were $C\infty$ (capacitance at infinite scan rate) represents the double-layer capacitance, C_0 denotes the total capacitance at lowes scan rates ($s = 1$ mV/s) including both double-layer and pseudocapacitive contributions, while k is the decay rate. DEL capacitance contribution as a percentage of the total capacitance was calculated as a ratio between $C\infty$ and C_0 (Fig.12).

The C-series exhibits relatively high DEL contributions (50-60 %) across all carbonization temperatures. In contrast, the CN-series shows lower DEL contributions, ranging 27-43 % with minimum observed for carbon synthesized at 800 °C. The decline in DEL contributions for the CN-series at intermediate temperatures suggests enhanced pseudocapacitive processes, while the increased contributions for CN900 sample indicate partial loss of effect of surface functional groups due the change of porose structure. These trends underline the synthesis-driven differences in charge storage mechanisms between the two series and their suitability for various applications. There is a positive correlation between specific surface area (S_{BET}) and double-layer capacitance ($C\infty$) with Pearson's $r = 0.90$ for C-series carbons. The absence of a similar dependency in the CN-series reflects the dominance of pseudocapacitive mechanisms and the complex interplay of structural and chemical properties affecting capacitance.

At the same time the estimation of DEL capacitance from the $C(s)$ dependence at high sweep rates is kinetically limited by ion accessibility to mesopores and external surfaces only with an incomplete representation of micropores contribution. At high sweep rate values the ion diffusion within the porous electrode becomes insufficient to keep up with the rapid potential changes that restrict ion accessibility to smaller or rather less connected pores, estimated for CN-series carbon materials.

These findings underline the critical role of synthesis methods in defining the charge storage mechanisms and the resulting performance characteristics of porous carbon materials. The C-series is optimized for stable double-layer capacitance applications, while the CN-series is tailored for pseudocapacitive behavior. The enhanced performance of the CN series materials underscores the critical role of chemical activation in tailoring the pore structure and surface properties to improve electrochemical behavior.

4. CONCLUSION

This study provides a comparative analysis of hemp fiber-derived porous carbon materials synthesized through steam-assisted carbonization (C series) and subsequent nitric acid activation (CN series). SAXS and nitrogen porosimetry data indicate greater surface heterogeneity and microporosity in the CN series compared to the C series. The evolution of fractal dimensions,

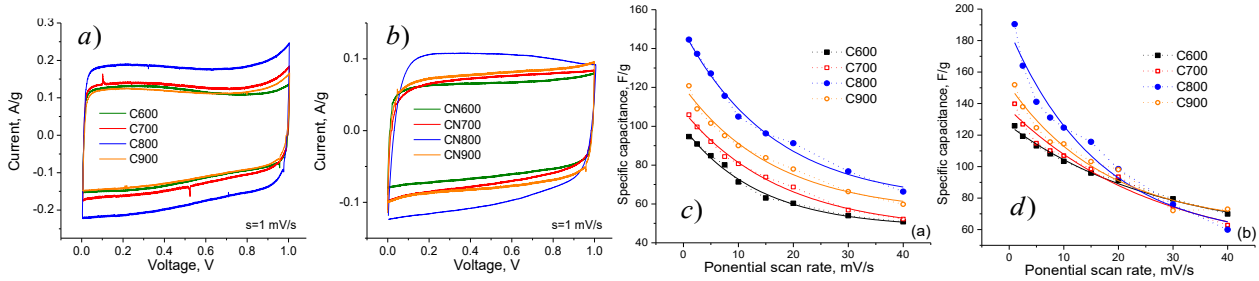

Fig. 11 – (a-b) CV curves measured for electrodes at scan sweep rate 1 mV/s (6 M aqueous KOH as electrolyte) and (c-d) the dependencies of specific capacitance on scan rate for electrodes based on C- and CN-carbons

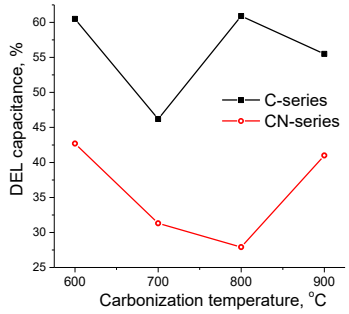

Fig. 12 – DEL capacitance contribution for electrodes based on the C- and CN-carbons

pore size and surface area distributions of synthesized materials was discussed. The positive correlation between SAXS and FHH-derived fractal dimensions was observed for C series at mesopores level of structural arrangement but not for CN-series with dominating of micropore. The coherent change of FHH fractal dimensions for C- and CN-series is observed for micropores. The CN-series materials are predominantly microporous and exhibit a much narrow centered around 2-3 nm pore size distribution compared to the materials of C-series which have mixed micro-mesostructure. Accordingly CV analysis the CN series materials displayed enhanced specific capacitance and good rate capabilities due to their optimized pore structure and surface functionalization. These properties enabled a substantial pseudocapacitive contribution. Conversely, the C series materials predominantly relied on double-layer capacitance, with higher DEL contributions across all temperatures. The CN series, with its high porosity, hierarchical structures, and significant pseudocapacitive behavior, is well-suited for high-performance energy storage, catalysis, and adsorption applications. The findings underscore the importance of tailoring synthesis methods to optimize the structural and functional properties of porous carbon materials using plant feedstock. The complementary use of XRD, SAXS, nitrogen porosimetry provides a robust framework for understanding and enhancing material performance across a wide range of applications.

REFERENCES

1. H.L. Tekinalp, E.G. Cervo, B. Fathollahi, M.C. Thies, *Carbon* **52**, 267 (2013).
2. C. Chen, K. Sun, C. Huang, M. Yang, M. Fan, A. Wang, J. Liu, *Biochar* **5** No 1, 51 (2023).
3. M.Y. Shen, W.Y. Liao, T.Q. Wang, W.M. Lai, *Sustainability* **13** No 4, 1788 (2021).
4. C. Qiu, L. Jiang, Y. Gao, L. Sheng, *Mater. Design* **230**, 111952 (2023).
5. E. Frackowiak, F. Beguin, *Carbon* **39**, 937 (2001).
6. D. Pantea, H. Darmstadt, S. Kaliaguine, L. Sümmchen, C. Roy, *Carbon* **39** No 8, 1147 (2001).
7. B.K. Ostafiychuk, R.P. Lisovskiy, A.H.Z. Al-Saedi, B.I. Rachiy, V.O. Kotsyubynsky, P.I. Kolkovsky, A. B. Hrubiak, *J. Nano- Electron. Phys.* **11** No 3, 03036 (2019).
8. M. Vukcevic, A. Kalijadis, M. Radisic, B. Pejic, M. Kostic, Z. Lausevic, M. Lausevic, *Chem. Eng. J.* **211**, 224 (2012).
9. M. Bembenek, V. Kotsyubynsky, V. Boychuk, B. Rachiy, I. Budzulyak, Ł. Kowalski, L. Ropyak, *Energies* **15** No 22, 8761 (2022).
10. R. Yang, G. Liu, X. Xu, M. Li, J. Zhang, X. Hao, *Biomass Bioenergy* **35** No 1, 437 (2011).
11. M.H. Reich, S.P. Russo, I.K. Snook, H.K. Wagenfeld, *J. Colloid Interface Sci.* **135** No 2, 353 (1990).
12. N. Ivanichok, P. Kolkovskyi, O. Ivanichok, B. Rachiy, D. Borchuk, R. Poveda, V. Boychuk, *Fullerenes, Nanotubes and Carbon Nanostructures* **31** No 9, 828 (2023).
13. K. Laszlo, A. Bota, L. Nagy, G. Subklew, M. Schwuger, *Colloids and Surfaces A: Physicochemical and Engineering Aspects* **138** No 1, 29 (1998).
14. K. Tanaka, A. Ito, T. Yoshii, S. Suehiro, S. Nagura, N. Ando, Y. Hato, *Carbon* **39** No 10, 1599 (2001).
15. V. Kotsyubynsky, B. Rachiy, V. Boychuk, I. Budzulyak, L. Turovska, M. Hodlevska, *Fullerenes, Nanotubes and Carbon Nanostructures* **30** No 8, 873 (2022).
16. L.F. Velasco, R. Guillet-Nicolas, G. Dobos, M. Thommes, P. Lodewyckx, *Carbon* **96**, 753 (2016).
17. F. Ambroz, T.J. Macdonald, V. Martis, I.P. Parkin, *Small Methods* **2** No 11, 1800173 (2018).
18. X.L. Zhou, H. Zhang, L.M. Shao, F. Lü, P.J. He, *Waste Biomass Valor.* **12**, 1699 (2021).
19. E. Härk, M. Ballauff, *C* **6** No 4, 82 (2020).
20. A.L. Ahmad, N.N.N. Mustafa, *J. Colloid Interface Sci.* **301** No 2, 575 (2006).
21. L. Xie, F. Su, L. Xie, X. Guo, Z. Wang, Q Kong, C. Chen, *Mater. Chem. Front.* **4** No 9, 2610 (2020).
22. S. Wabo, O. Klepel, *Carbon Lett.* **31** No 4, 581 (2021).
23. B. Daffos, P.L. Taberna, Y. Gogotsi, P. Simon, *Fuel Cells* **10** No 5, 819 (2010).
24. P. Forouzandeh, V. Kumaravel, S.C. Pillai, *Catalysts* **10** No 9, 969 (2020).

Адаптація пористого вуглецю, отриманого з конопель, шляхом хімічної активації: аналіз фрактальної розмірності та ємнісні властивості

Р.І. Запухляк, В.О. Коцюбинський, В.М. Бойчук, В.Т. Гой, М.М. Клим'юк

Карпатський національний університет імені Василя Стефаника, 76018 Івано-Франківськ, Україна

У роботі досліджено структурні та електрохімічні властивості пористих вуглецевих матеріалів, отриманих з конопляних волокон, синтезованих за допомогою карбонізації (серія C) та активації азотною кислотою (серія CN). Серія CN демонструвала вищу мікропористість та вузький розподіл розмірів пор (з центром близько 2-3 нм), тоді як серія C демонструвала ширшу мікромезопористу структуру. Фрактальні розміри, розраховані за допомогою методів SAXS та FHH, показали послідовні тенденції, причому серія C виявила позитивну кореляцію на рівні мезопор, а серія CN підкреслила домінування мікропористих структур. Електрохімічні оцінки показали, що матеріали серії CN досягають високих питомих ємностей та швидкісних характеристик завдяки оптимізованій структурі пор та функціоналізації поверхні, що забезпечує значний псевдоємнісний внесок. На противагу цьому, серія C в основному спиралася на двошарову ємність, що підтримувалося її змішаною мікромезопористою структурою. Дослідження підкреслює вплив методів синтезу на адаптацію архітектури пор та функціональних характеристик, надаючи розуміння розробки пористих вуглецевих матеріалів для передових застосувань, таких як накопичення енергії, каталіз та адсорбція.

Ключові слова: Пористий вуглець, SAXS, Порометрія, Фрактальна розмірність, Розподіл пор, Питома ємність.